Using the Special Sensor Microwave/Imager to Monitor Land Surface Temperatures, Wetness, and Snow Cover

ALAN BASIST

Global Climate Laboratory, National Climatic Data Center, National Environmental Satellite, Data and Information Service, National Oceanic and Atmospheric Administration, Asheville, North Carolina

NORMAN C. GRODY

Office of Research and Applications, National Environmental Satellite, Data and Information Service, National Oceanic and Atmospheric Administration, Camp Springs, Maryland

THOMAS C. PETERSON AND CLAUDE N. WILLIAMS

Global Climate Laboratory, National Climatic Data Center, National Environmental Satellite, Data and Information Service, National Oceanic and Atmospheric Administration, Asheville, North Carolina

(Manuscript received 26 February 1997, in final form 5 December 1997)

ABSTRACT

The worldwide network of in situ land surface temperatures archived in near-real time at the National Climatic Data Center (NCDC) has limited applications, since many areas are poorly represented or provide no observations. Satellite measurements offer a possible way to fill in the data voids and obtain a complete map of surface temperature over the entire globe. A method has been developed to calculate near-surface temperature using measurements from the Special Sensor Microwave/Imager (SSM/I). To accomplish this, the authors identify numerous surface types and make dynamic adjustments for variations in emissivity. Training datasets were used to define the relationship between the seven SSM/I channels and the near-surface temperature. For instance, liquid water on the surface reduces emissivity; therefore, the authors developed an adjustment to correct for this reduction. Other surface types (e.g., snow, ice, and deserts) as well as precipitation are identified, and numerous adjustments and/or filters were developed for these features. The article presents the results obtained from training datasets, as well as an independent case study, containing extreme conditions for deriving temperature from the SSM/I. The U.S. networks of first-order and cooperative stations, quality controlled by NCDC, serve as validation data. The correlation between satellite-derived and in situ temperatures during the independent case (''Blizzard of 1996'') was greater than 0.95, and the standard error was 2°C. The authors also present SSM/I-derived snow cover and wetness maps from this 2-week period of the blizzard. A prototype for blending the satellite and in situ measurements into a single land surface temperature product is also presented.

1. Introduction

Temperatures measured 2 m above the ground (referenced as surface temperatures in this article) are used for numerous purposes, such as monitoring regional anomalies and climate variability (e.g., Trenberth et al. 1992). Global circulation models (GCMs) need gridded surface temperature as a primary input for initialization and validation of climate simulations. Hydrologists need surface temperatures to gauge the supply and demand of surface water resources (Lettenmaier 1994). For instance, surface temperature regulates snowmelt for irrigation and reservoirs. Surface temperatures also determine the rate of crop development and water demand in agriculture. They are also central to studies of radiation budgets, a topic under intensive study by the World Climate Research Program. These are only a few examples of the potential application of a global land surface–temperature dataset. Furthermore, a land surface temperature product could be merged with a blended sea surface temperature dataset (Reynolds and Smith 1994) to produce a global surface temperature product.

Although surface temperature is a key element of weather and climate, there has never been an adequate network of in situ measurements to provide detailed global analysis of this parameter. A map from the Annual Assessment of the Climate Prediction Center (Halpert 1994) illustrates where the surface temperatures are inadequate (Fig. 1). It shows data-void areas over most

Corresponding author address: Alan Basist, GCL, NCDC, Room 120, 151 Patton Avenue, Asheville, NC 28801.
E-mail: abasist@ncdc.noaa.gov

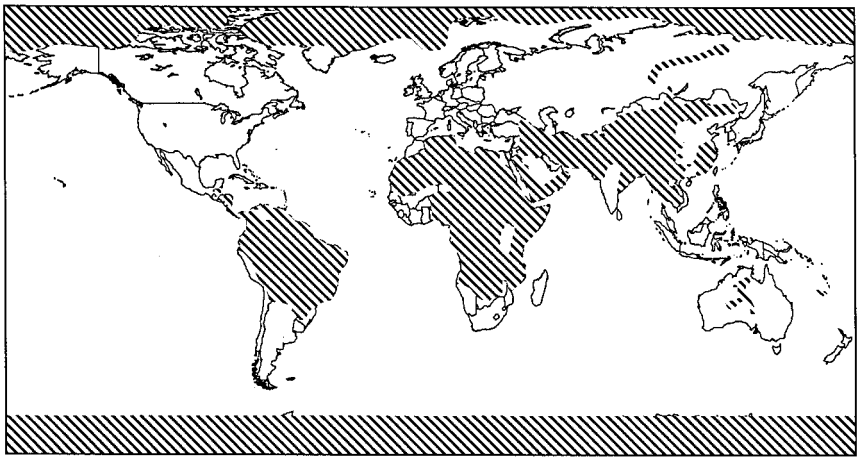

FIG. 1. Hatched areas indicate where adequate surface temperature observations were unavailable in 1994 (Halpert 1994). The Reynolds and Smith (1994) blended SST product provided anomalies over most of the global oceans, whereas the continents have major holes where in situ measurements are scarce. We intend to reduce the extent of these areas with a blended land surface temperature product.

of Africa, South America, southern Asia, and over all of Antarctica. Temperature data are too sparse in these areas to adequately interpolate annual anomalies. In addition, there is limited confidence in the interpolated values over high terrain, since the station measurements are usually in the inhabited valleys, which do not represent the mean regional temperature. Karl et al. (1994) clearly state the importance of monitoring global temperatures: ''Our results point to the critical need for a well-conceived global network of surface-based observing stations if we ever hope to obtain highly reliable estimates of surface boundary layer temperature trends. The urgency of this effort is underscored by the absence of space-based monitoring of the surface-layer diurnal temperatures.'' In response to this need we developed an algorithm that determines temperatures from the Special Sensor Microwave/Imager (SSM/I). This technique builds on the experience by Grody and Basist (1996), who were able to monitor the global distribution of snow cover from the same satellite instrument.

In order to derive the surface temperature in the microwave spectrum, the variation in surface emissivity must be addressed. The major factor influencing the variation in emissivity is surface wetness, which at 19 GHz (vertical polarization) can lower emissivity by 33%. Therefore, it is necessary to quantitatively determine the perturbation due to surface wetness on the brightness temperature measurements when deriving surface temperature. Consequently, this article investigates the use of SSM/I measurements for monitoring both land surface temperature and wetness.

High density in situ measurements over the United States serve as validation of the temperature algorithm. However, there are intrinsic differences between the in situ temperatures, which are measured at 2 m above a grass surface, and the satellite brightness temperature (T_b) from a radiating surface (e.g., the canopy and/or soil). The wetness index, described in detail below, measures the fractional amount of liquid water in the radiating surface observed by a SSM/I footprint. Microwave frequencies used in this study do not penetrate more than a centimeter into the soil nor do they penetrate through dense vegetation; therefore, the wetness index should not be confused with soil moisture, since one cannot assume that surface and subsurface are coupled.

The paper is divided into six additional sections. Section 2 explains the history of satellite-derived land surface temperature products, followed by the strengths and weaknesses of using microwave frequencies to derive this parameter. Section 3 describes the procedures used to (a) classify land surface types, (b) adjust for variable emissivity, and (c) derive the surface temperature. A technique to identify wet ground based on the emissivity adjustment is also introduced. Section 4 compares high density in situ temperature data from the U.S. Cooperative Network with the satellite product over the United States during July 1992. The wetness and temperature fields will be analyzed, and satellite temperatures will be compared against in situ observations. Section 4 also contains a comparison of the satellite-derived products (temperature, wetness, and snow cover) with independent data during a 2-week period of extremely adverse conditions, the Blizzard of 1996. Section 5 tests the benefits of blending in situ and satellite temperatures into one product. Section 6 is reserved for a concluding summary and a short description of future work.

2. History of satellite-derived surface temperature

The determination of surface temperature from satellite radiometer measurements has been attempted using different spectral regions. Under ideal conditions,

where the atmospheric absorption is negligible and the surface emissivity is constant, radiometric measurements are directly proportional to surface temperature. However, in the infrared region one must account for the atmospheric absorption due to clouds and water vapor in addition to small variations in surface emissivity. At the much longer microwave wavelengths the effects of atmospheric absorption can often be neglected over land, although one must account for the variations due to surface emissivity. As such, it is important to develop a combined product where infrared measurements are used under clear conditions, and emissivity adjustments are calculated for the microwave measurements. Presently, much of the emphasis has focused on the use of infrared measurements for deriving surface temperature. This stems from the fact that until recently, microwave sensors did not contain a sufficient number of window (i.e., surface) channels to adequately correct for emissivity variations. Before describing the microwave technique, a brief history of the use of satellites for deriving surface temperature is given.

a. Infrared

There have been several attempts to derive a global field of near-surface temperatures (2 m above the ground) from satellite observations. Initially, infrared sensors were used to monitor the temperature near the surface (Davis and Tarpley 1983). However, clouds absorb and reradiate infrared energy, which limits the technique to cloud-free areas (Rizzi 1994). Significant efforts have been made to separate out clouds from clear portions of the infrared observations. However, the final product still contains some residual cloud contamination and pervasive clouds cause data voids over large areas (Cornett and Shank 1993). Additional unresolved issues (such as atmospheric water vapor) are discussed by Hall et al. (1992). Most of the previous studies relied heavily on the infrared instruments, and standard errors for surface temperature ranged around 3°C (Rossow and Garder 1993; Vidal 1991; Myneni and Choudhury 1993). Therefore we are pursuing a different approach that results in smaller errors.

b. Passive microwave

Passive microwave emission penetrates nonprecipitating clouds, thereby providing a better representation of surface temperatures under nearly all sky conditions. This study uses data from the SSM/I to infer atmospheric and surface parameters. The SSM/I flown by the Defense Meteorological Satellite Program (DMSP) contains seven channels: four with vertical (V) polarization (19, 22, 37, and 85 GHz), hereafter called 19V, 22V, 37V, and 85V; as well as three with horizonal (H) polarization (19, 37, and 85 GHz), hereafter called 19H, 37H, and 85H. Hollinger et al. (1987) reviewed the various algorithms used to derive surface and atmospheric parameters from this instrument. McFarland et al. (1990) noted serious limitations in deriving temperature over several surface types, including snow cover and wet ground.

Over land, passive microwave observations are primarily a function of surface emissivity and temperature (outside of deep convection there is little atmospheric interference over land at 19V). In order to derive surface temperature it is necessary to adjust for surface emissivity variations (Jones and Vonder Haar 1997). Matzler (1994) described the spectral and polarization variation of emissivity for different winter surface types, including bare soil, wet ground, shallow snow, metamorphosed snow, crusted snow, and grass. Most of the surface types can be identified by their unique spectral signatures, although some ambiguities exist. He found that many surfaces exhibited small variations in emissivity at certain frequencies, an important finding when developing algorithms for deriving surface temperature. Njoku (1994) found that remotely sensed microwave emission has a stronger empirical relationship to surface temperature than theory implies. The empirically derived atmospheric contribution is generally smaller, and the correlations between emissivity at different frequencies are more stable than theoretical simulations suggest. In order to minimize the variations associated with surface emissivity, only the vertically polarized SSM/I channels were used to derive surface temperature.

3. Methodology for deriving SSM/I surface temperature

a. Procedure

Ferraro et al. (1996) showed how passive microwave measurements can be used to successfully monitor numerous atmospheric (i.e., cloud liquid water, precipitation, and precipitable water) and surface parameters (i.e., winds over oceans, sea ice concentration, and snow cover). These parameters are determined using the frequency and polarization characteristics of surface emissivity and atmospheric transmission. Neale et al. (1990) developed a series of algorithms to identify various land surface types, based on the unique signatures of the SSM/I channel measurements. He was able to discriminate between dense vegetation, rangeland, wet surfaces, semiarid soils, and desert. Grody and Basist (1996, 1997) analyzed SSM/I observations and developed a decision tree that associates various surface features (i.e., snow cover, deserts, frozen ground, vegetated surfaces, rain, and glaciers) using specific relationships between the SSM/I channel measurements. In addition to this work, they were able to identify wet and dry ground; that is, for wet surfaces the brightness temperature (T_b) increases with frequency and there is a large polarization difference (Tsang et al. 1993), whereas for dry and veg-

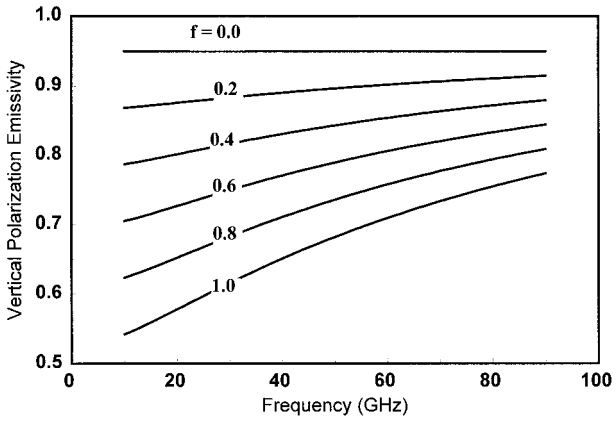

FIG. 2. A theoretical relationship of emissivity over a spectrum of microwave frequencies for six different magnitudes of surface wetness. The top curve corresponds to 0% of the surface covered with water, and the bottom curve corresponds to 100% of the surface covered by water. Note how the slope of the curve changes as the fractional amount of surface water increases.

etated surfaces the T_b has a small variation with frequency and little polarization difference.

To formulate a surface temperature algorithm, we express the brightness temperature measurement as

$$T_b(\upsilon) = \epsilon_s(\upsilon)T_s, \tag{1}$$

where T_b is the brightness temperature at frequency υ, ϵ_s is the surface emissivity, and T_s is the surface temperature. This equation assumes negligible atmospheric effects over land compared to the variations in surface temperature and emissivity. Since the smallest variation in emissivity occurs for vertical polarization, this polarization is preferred when deriving surface temperature.

Corrections for variations in surface emissivity due to wet surfaces can be obtained using additional channel measurements. When the ground is dry the vertically polarized SSM/I channels have a nominal emissivity ϵ_0 of 0.95. However when the surface is wet, the emissivity can be written as

$$\epsilon_s(\upsilon_1) = \epsilon_0 - \Delta\epsilon, \tag{2}$$

which contains the nominal emissivity over dry ground and the change of emissivity $\Delta\epsilon$ at frequency υ_1 due to surface wetness, which can be expressed as

$$\Delta\epsilon = f(\epsilon_0 - \epsilon_w), \tag{3}$$

where **f** is the fractional amount of the radiating surface that is liquid water and the emissivity of dry ground and liquid water is ϵ_0 and ϵ_w, respectively.

Wang and Schmugge (1980) developed a model for computing the emissivity of wet surfaces based on the dielectric constant of water (which increases with frequency) and the field capacity of the soil. The lowest emissivity occurs when the surface becomes saturated with water, as in the case of flooded land (Entekhabi et al. 1995). Figure 2 shows how emissivity over a surface changes in (2) and (3) as a function of frequency and the parameter **f**. As the fractional amount of wet land increases, the emissivity decreases and the slope of emissivity between low and high frequencies increases. This feature is also demonstrated in Fig. 3. Figure 3a shows the location of the cross section over the Mississippi valley, and Fig. 3b shows the value of SSM/I measurements in the cross section. Values at the four frequencies decrease as the fractional amount of wetness increases. (Note that **f** is maximum over the portion of the cross section where the Mississippi River resides.) Also observe that the largest reduction in the values occurs for the lowest frequency channel (19 GHz), and that the difference between the high and low frequency measurements (i.e., slope) increases with **f**.

From the above results, it is evident that the decrease in emissivity in (2) can be related to the slope of emissivity between two or more frequencies and is approximated as

$$\Delta\epsilon = \beta_0[\epsilon_s(\upsilon_2) - \epsilon_s(\upsilon_1)] + \beta_1[\epsilon_s(\upsilon_3) - \epsilon_s(\upsilon_2)], \tag{4}$$

where υ_1, υ_2, and υ_3 represent the 19V, 37V, and 85V channels, respectively. Since the frequency variation in emissivity for wet surfaces is nonlinear (see Fig. 2), the emissivity correction contains two sections with different proportionality constants (β_0 and β_1), which accounts for the decreased slope at high frequencies (Fig. 2). Furthermore, the fields of view (FOVs) at the various frequencies range from 60 km at 19 GHz to 15 km at 85 GHz, and the two proportional constants in (4) partially account for this variation.

Substituting (2) and (4) into (1) and solving for T_s, we obtain

$$T_s = (1/\epsilon_0)\{T_b(\upsilon_1) + \beta_0[(T_b(\upsilon_2) - T_b(\upsilon_1)] + \beta_1[(T_b(\upsilon_3) - T_b(\upsilon_2)]\}. \tag{5}$$

The functional form of $\Delta\epsilon$ was empirically determined from global SSM/I measurements and surface temperatures over wet and dry land. These measurements include a myriad of climatological conditions, for example, river valleys adjacent to dry ground, irrigated regions adjacent to nonirrigated areas, melting snow next to snow-free ground, and recent rain-soaked ground near dry ground. To minimize external factors, we conscientiously chose sites where the surface characteristics are internally homogeneous and where there is nominal topographic gradient. To maximize external factors, we used sites from all over the world, at all times of the year, from both morning and afternoon passes. A scatter diagram between the expected and predicted surface temperature had a correlation coefficient of 0.95 and a standard error less 2.5°C (Basist and Grody 1997). Since these are individual pixel errors, the standard error would further diminish when mean monthly values over $1° \times 1°$ boxes are determined. In addition to computing the surface temperature, a new parameter called the Basist wetness index (BWI) is also derived. This parameter is defined as $\Delta\epsilon^* T_s$ that based on (4) becomes

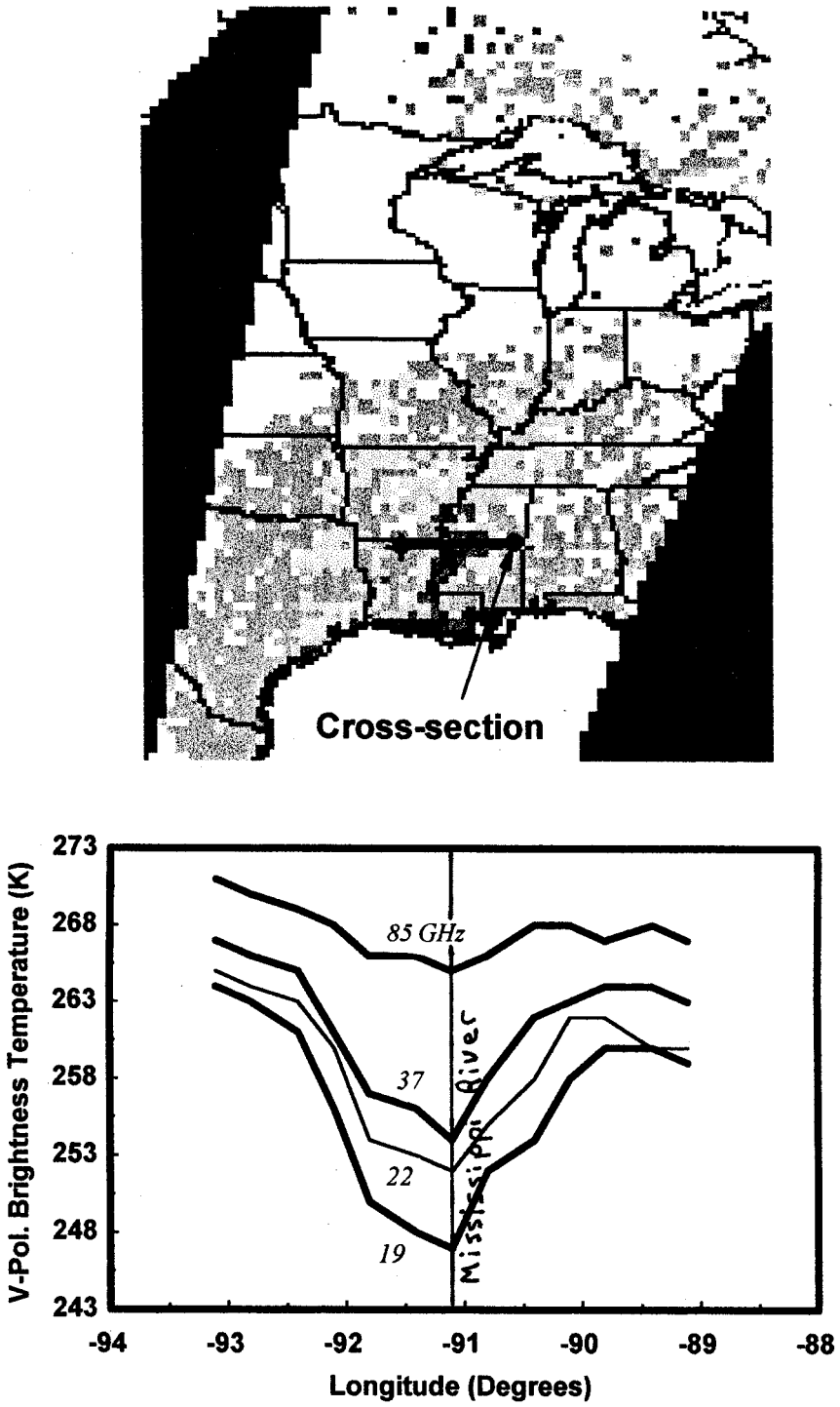

FIG. 3. (a) A map of the wetness index values through Mississippi flood plains during a descending pass on Julian day 38, 1996. (b) A cross section depicted by the bar in (a) corresponds to the four vertically polarized channels (19, 22, 37, and 85 GHz) measurements. Note the depression in temperature at the various frequencies as the bar crosses the Mississippi flood plain.

$$\text{BWI} = \Delta\epsilon^* T_s = \beta_0[(T_b(\upsilon_2) - T_b(\upsilon_1)] + \beta_1[(T_b(\upsilon_3) - T_b(\upsilon_2)], \quad (6)$$

so that (5) may be written as

$$T_s = (1/\epsilon_0)\{T_b(\upsilon_1) + \text{BWI}\}, \quad (7)$$

where the BWI is the brightness temperature correction at 19V due to surface wetness. According to (3), the wetness index is proportional to the amount of the radiation surface that is wet within the SSM/I FOV. To be more specific, we consider two extreme cases, bare and forested areas. For bare open areas the BWI represents the fraction of wet areas within the FOV. In the case of forests, the index corresponds mainly to the fraction of open areas that are wet or flooded, although water intercepted by the canopy is also observed. An additional contribution can arise in forests and vegetated areas when the canopy is covered with dew. However, this contribution is highly diurnal, being largest in the early morning, and is expected to be small in general. It should be noted that streams, rivers, and lakes contribute significantly to the wetness index when they occupy portions of the viewing area ''seen'' by the SSM/I.

Although we present the wetness value as an adjustment in the temperature field, it can also easily be viewed in other terms. If one rearranges (7) into (8),

$$\Delta\epsilon = \text{BWI}/T_s, \quad (8)$$

where the BWI represents the wetness index and T_s the wetness corrected temperature, then $\Delta\epsilon$ is the reduction in emissivity due to the liquid water in the radiating surface. Furthermore, if one considers (9),

$$f = (1 - (T_b/T_s))/0.33, \quad (9)$$

where T_b is the observed 19V brightness temperature, T_s is the wetness corrected 19v brightness temperature from (7), and 0.33 is the empirically derived range of emissivity between a completely wet and a completely dry surface, then **f** is the fractional amount of the radiating surface that is liquid water.

A procedure similar to (7) was used to make temperature adjustments over snow-covered surfaces. However, the emissivity correction depends on snow stratigraphy. Specifically, fresh (low density unmetamorphosed) snow does not scatter much, due to its low volume and small flake size (Grody and Basist 1997). Under these conditions $\Delta\epsilon$ is approximately zero, so that the 19V represents the ground temperature below the snow surface. In contrast, when snow goes through metamorphosis, the grains become larger and more dense (Matzler 1994), and radiation at all SSM/I frequencies is scattered. Frozen rain (which forms an ice coating over a vegetated surface) scatters radiation with nearly the same intensity at all SSM/I frequencies. The large ice features reduce the emissivity to approximately 0.90 with a slightly higher emissivity at 85 GHz. This decrease in emissivity at low frequencies results in a cold bias in the derived surface temperature. Fortunately, the three conditions described above have a unique signature, allowing them to be filtered from the temperature analysis. Corrections for snow and ice conditions are currently under investigation.

b. Satellite characteristics

The *F-11* satellite on the DMSP platform has a morning pass around 0600 LT and an afternoon pass around at 1800 LT. These passes were processed separately. The morning passes were compared against mean monthly minimum temperatures and the afternoon passes were compared against mean monthly maximum temperatures. Fortunately, at 0600 the satellite observation and in situ minimum temperatures are very close, since the lower boundary layer has approached an equilibrium state (Groisman and Genikhovich 1997). This allows for a more direct comparison between the in situ and satellite temperatures, since they are the closest at this time.

Unfortunately, there are incompatibilities between the time of the satellite observation and the occurrence of maximum temperature. Furthermore, various surface types and terrains have significantly different diurnal temperature curves and the limited in situ stations may not represent the diurnal pattern over a larger area. Consequently, it can be difficult to adjust the 1800 satellite T_b to the maximum temperature. Realizing that the primarily objective of this study is to identify the correct temperature gradients and patterns, we used a simple adjustment to bring satellite observation closer to the maximum temperature. Latitudinally, the largest diurnal cycle is generally over the low latitudes, where the period of daylight remains near 12 h; conversely, the smallest diurnal cycle occurs over the poles, where it is either illuminated or dark throughout the day. Therefore our current procedure uses the equation

$$T_b' = T_b \times [1 + 0.02 \times \cos(\theta)], \quad (10)$$

where θ serves as the latitude adjustment and T_b' is the cosine-adjusted brightness temperature for all SSM/I channels. Assuming a surface temperature of 300 K, the adjustment between the satellite observation and the maximum temperature adjustment can reach 6 K at the equator.

The SSM/I detects the temperature in the radiating surface, which can contain bare ground, water, vegetation, etc. Therefore, the origin of radiation observed by the SSM/I instrument can give a significantly different temperature than the in situ value measured 2 m above the ground. This difference is most pronounced over dry barren ground in the afternoon, where there can be a strong lapse rate in the lower 2 m. Fortunately by 1800 this superadiabatic lapse rate is diminishing, although it can still introduce considerable errors in the derived temperature field.

c. Processing the data

Our research has shown that the 19V has an emissivity of 0.945 over most dry ground and vegetated surfaces. Therefore the expected values of 19V are further multiplied by 1.06 (i.e., $1/\epsilon_s$) to obtain the surface temperature. Over deserts, minerals such as quartz and limestone have been identified using passive microwave measurements (Allison 1977). Based on dielectric constant values, quartz has an emissivity approaching 0.98 while the emissivity of limestone can drop to about 0.92 for this channel (Cambell and Ulrichs 1969). Theoretical and empirical analyses indicates that the temperature at the 22V water vapor will be colder than the 19V window channel when the emissivity exceeds 0.95; conversely the temperature at 22V and 85V (another channel sensitive to water vapor) will be higher than 19V and 37V (window channels) when the emissivity drops below 0.95. Frequency and polarization information from these channels has been used to identify the composition of the radiating surface over deserts. Knowing the composition of the surface, we have developed an adjustment for the increased emissivity due to quartz by using the 22V channel value. Unfortunately, no adjustment is currently available for limestone. Therefore, these areas are filtered from the analysis. As discussed above, most snow-covered surfaces are removed from the analysis using the algorithm developed by Grody and Basist (1997) to identify snow cover. The scattering signature associated with deep convection (Ferraro and Marks 1994) is used to remove these areas from the analysis. Furthermore, flooded land is filtered out, since the BWI is not applicable under exceedingly wet conditions; errors in the adjusted emissivity become excessive when the polarization difference between 19V and 19H exceeds 45°C (when the FOV is dominated by water). A simplified decision tree is presented in Fig. 4, it illustrates our approach in using the seven channels of the SSM/I instrument to identify surface temperature, filter out several parameters, and correct for variable emissivity. At the end we plan to adjust these surface temperatures to shelter height observations, by blending with in situ measurements.

The daily satellite data has been processed into ⅓° resolution grids, which is approximately the footprint size for the 37-GHz channel and this archive is maintained in National Environmental Satellite, Data and Information System (NESDIS) (Ferraro et al. 1994). All the processing and adjustments for deriving land surface temperatures are performed on a pixel resolution for daily ascending and descending orbits. The satellite-derived temperatures are averaged into monthly, 1° resolution grid boxes. A grid box must have observations from at least half the month, otherwise the grid is set to missing. The large number of spatial and temporal observations averaged into these monthly fields reduces the random error contained in the daily high resolution data.

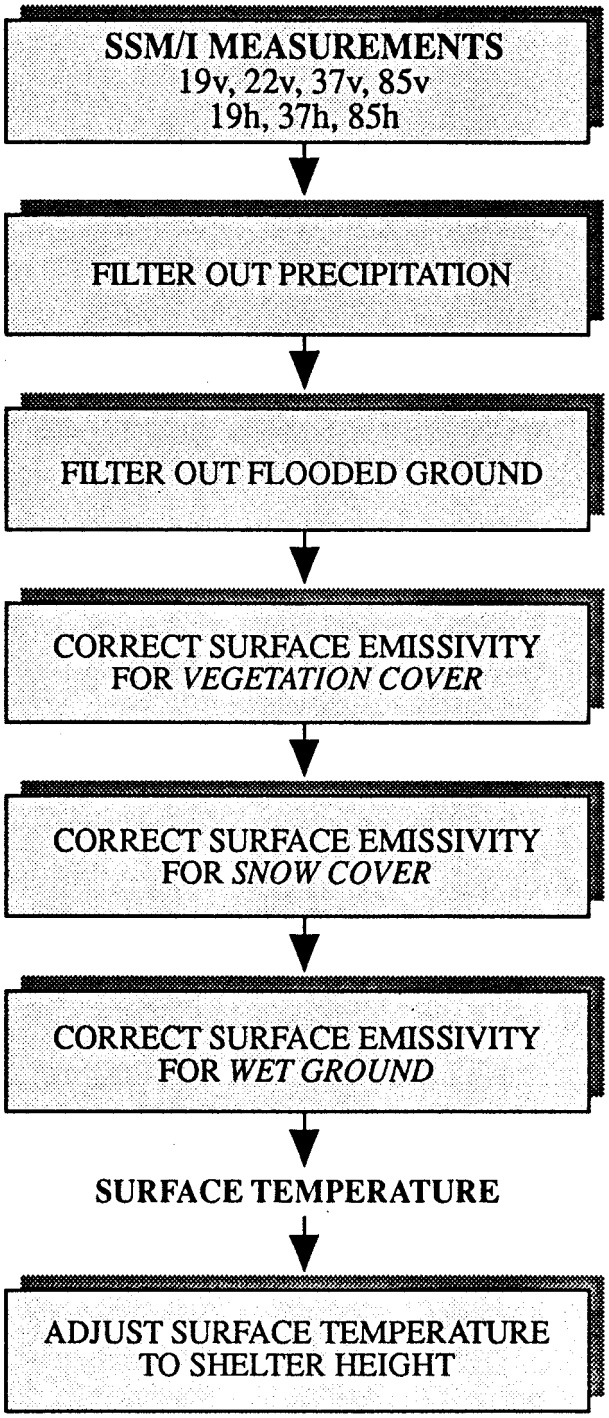

FIG. 4. A schematic of the ''prototype'' decision tree used to translate the SSM/I channel values to shelter height temperatures.

A network of more than 5000 cooperative stations report shelter height temperatures throughout the United States. This network is quality controlled and archived at the National Climatic Data Center. These data are used to validate the accuracy of our procedure to simulate shelter height maximum and minimum tempera-

tures from the SSM/I instrument (it is one of the most extensive and densest networks of in situ stations available on a national scale). The in situ data are interpolated into 1° resolution on a monthly timescale (using the software developed at the National Centers for Environmental Prediction for operational purposes), and these gridded fields are directly compared to the satellite-derived temperatures at the same resolution. Maximum and minimum temperatures are processed separately, and these values are correlated against data from the morning and afternoon satellite passes. No correction for elevation was added to the in situ data at this time. Therefore, over mountainous areas the stations frequently do not represent the temperature of the 1° pixel, causing a cold bias. In the following section the satellite and in situ data are presented separately, followed by difference fields and other statistics on their relationship.

4. Satellite–in situ comparison

Independent validation of the satellite-derived snow cover and temperature during the Blizzard of 1996 is provided by the first-order weather station data (available in real time from the National Weather Service), and the weekly snow cover product (available in near-real time from NESDIS). This network of synoptic reporting stations is not nearly as dense as the cooperative network, but 300 stations provide a reasonable representation of the temperature distribution in the eastern United States. Since this is where the Blizzard of 1996 deposited a tremendous amount of snow, which rapidly melted the following week, it provides an excellent opportunity to test the accuracy of our satellite-derived temperatures and the adjustments under extreme conditions.

a. Maximum temperature in July 1992

The monthly mean maximum temperatures during 1992 are gridded and plotted from the 5000 in situ stations across the United States (Fig. 5b). They have a distinct north to south gradient, with the highest temperatures in the desert southwest and the coldest temperatures in the Rocky Mountains. The satellite-derived maximum temperatures have a similar structure (Fig. 5a) but with noticeable differences. The satellite observes a band of cool temperatures down the Appalachian Mountain range, which is absent in the in situ observations since they lack measurements from ''high elevation'' remote areas. The satellite also identifies distinctly colder temperatures over the high elevations of the Sierra Nevada of eastern California, where in situ observations are severely limited. A map of the difference between the two temperature fields clearly demonstrates that the satellite product has lower temperatures along the Appalachian Mountains, as well as the mountain ranges of the western United States (Fig. 6). There are other positive biases in regions of the country where the in situ values should be quite reliable, such as the Midwest and Great Lakes regions. We attribute these differences to errors and/or biases in the satellite-derived temperature. (For instance, a few of the warmer days of the month could have occurred in satellite gaps, which would introduce a cold bias over the region.) The satellite has higher temperatures in southern Arizona and California. A map of the in situ values (Fig. 7) indicates that there are limited observations in the desert southwest, which is an extremely hot region. Therefore, the interpolation scheme places erroneous temperatures over the area and the satellite temperatures are probably more realistic.

The correlation coefficients (r) between the two maps (Figs. 5a and 5b) is 0.90 with a root-mean-square difference (rms) of 1.98°C. Differences generally originate from three sources: the satellite data emissivity adjustment, gradients between the radiating surface and shelter height temperature, or the in situ values are not representative of the 1° grid. This last difference could be significantly reduced using a Digital Elevation Map and a lapse rate adjustment to transform the in situ measurements to values better representing the mean areal elevation of the grid box.

Over a limited area in the center of the country, where there are small gradients in elevation and a high density of in situ values, the correlation is 0.96 and the rms drops to 1.57°C. These errors could be further reduced by effective blending of the two fields into a final product. The in situ values would provide the anchor and the satellite would provide the gradient. The satellite product would be particularly valuable over areas of the world where in situ values are sparse. A global map of the satellite-derived, maximum temperatures for July 1992 shows many features that would be hard to capture from in situ measurements alone (Fig. 8). The topographic structure of the Tibetan and Ethiopian Plateaus, and numerous mountain ranges, such as the Andes and Caucasus, are evident in this map. Also, a distinct north–south temperature gradient in Australia, Africa, and South America is observed during their winter season. High temperatures over the Northern Hemisphere deserts stand out, as well as cold temperatures in the Arctic. Glacial ice over Antarctica and Greenland and limestone surfaces over Africa, southern Asia, and Australia have been filtered out of the analysis.

The BWI field has some strong gradients, which frequently exceed a value of 6 across a small area (Fig. 9). Nonetheless, when the BWI gradients are added to T_b (in order to correct for emissivity reduction) no corresponding ''bull's-eyes'' in the temperature pattern are apparent, which strongly suggests that the index correctly adjusts for wetness. Generally, higher wetness values are observed over the eastern half of the country, which receives more rain at this time of year. The satellite observes wetness over cultivated areas, this wetness is probably observed between plants and/or on the

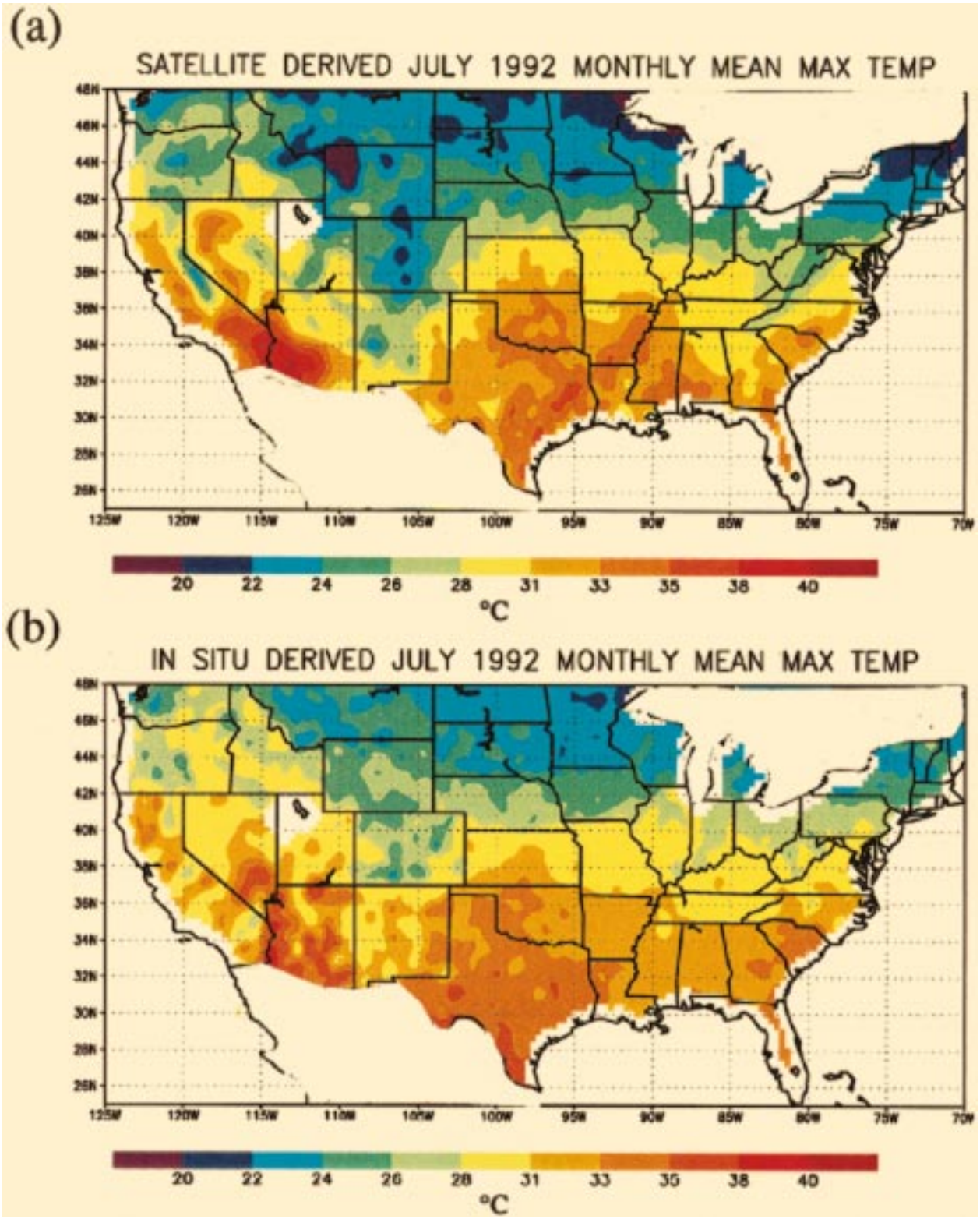

FIG. 5. (a) Satellite-derived maximum temperatures for the month, derived from the SSM/I channel measurements. Note the smooth structure of the satellite grid over flat land, and the gradients over the Appalachian, Sierra Nevada, and Rocky Mountains. (b) In situ shelter height, maximum temperatures from the U.S. Cooperative Network gridded at 1° resolution for July 1992.

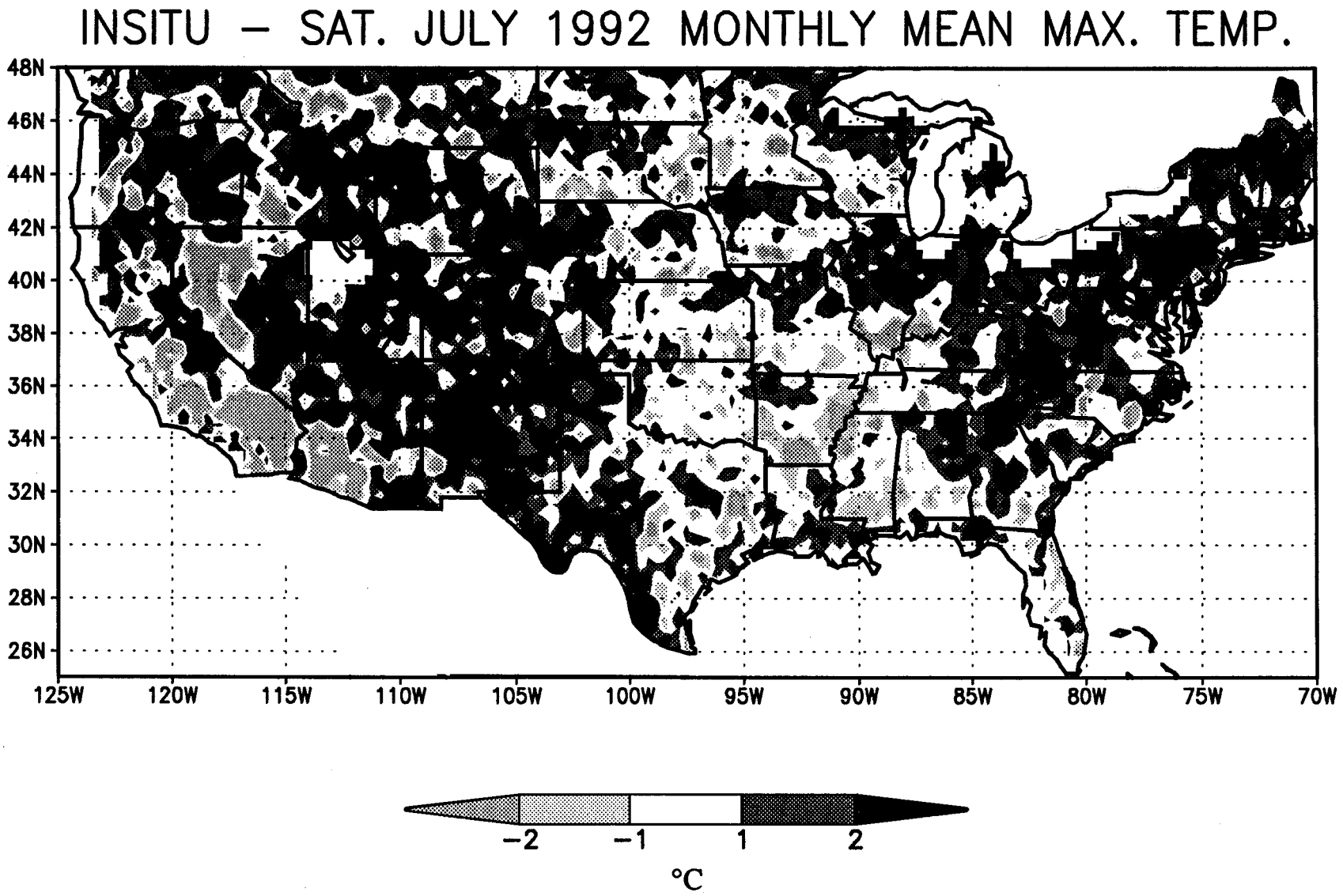

FIG. 6. Spatial differences between in situ and satellite-derived shelter-height temperatures for July 1992 maximum temperature. Positive (negative) values correspond with higher in situ (satellite) temperatures.

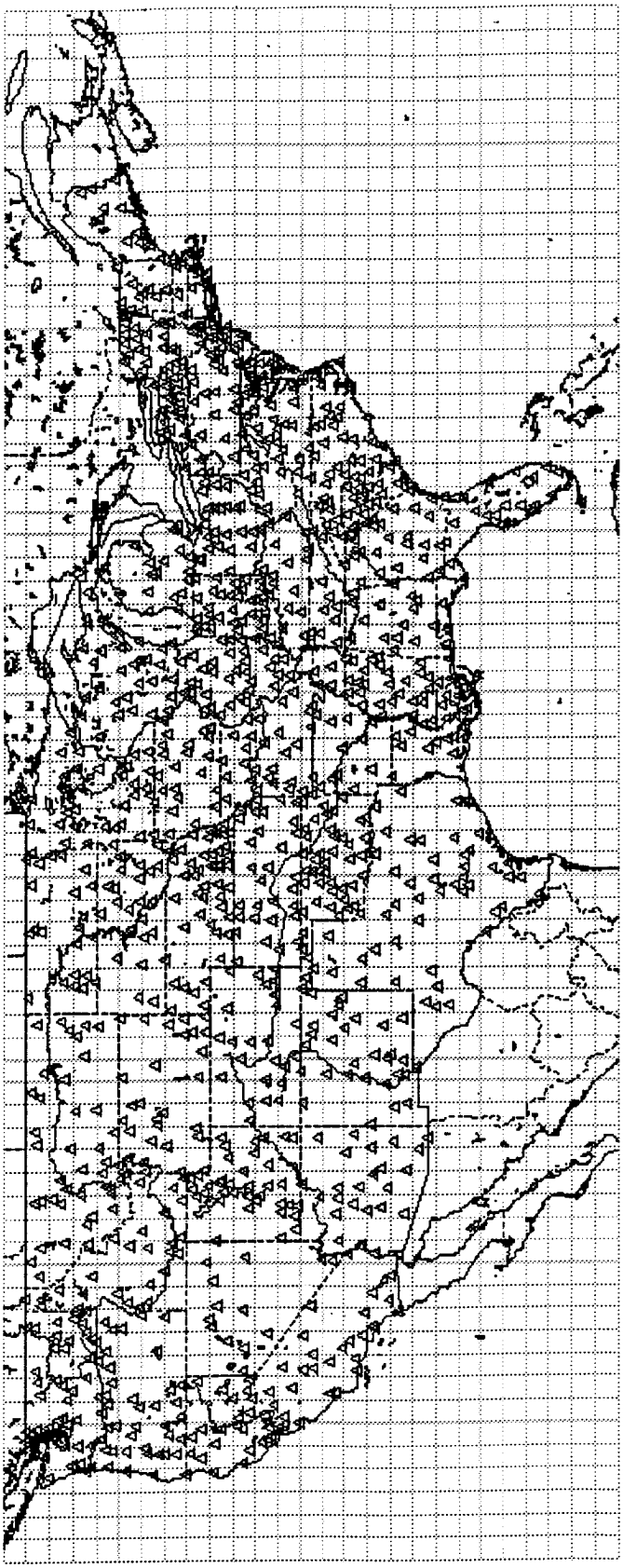

FIG. 7. A map of the 5000 in situ stations used as ground truth for the satellite temperature product. The greatest distribution occurs over the eastern two-thirds of the county. Note the sparsity of data over remote areas of the western states, where the greatest differences occur.

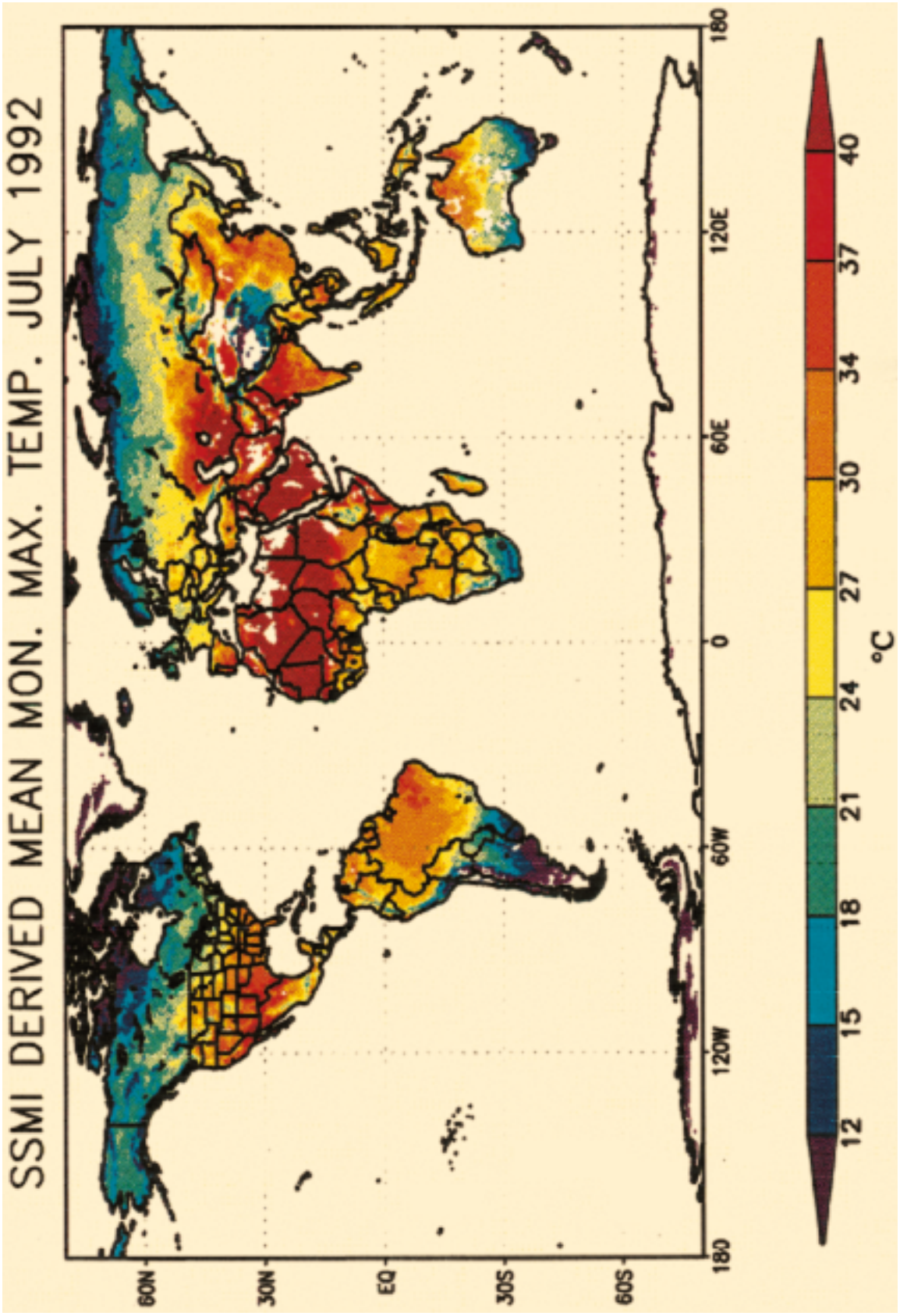

FIG. 8. A global field of satellite-derived temperatures, which is produced at 1° resolution for July 1992. Note the strong temperature gradients during the Southern Hemisphere winter, and areas of high terrain (Tibet, Andes, and Alps), as well as the smooth field over the tropical forests.

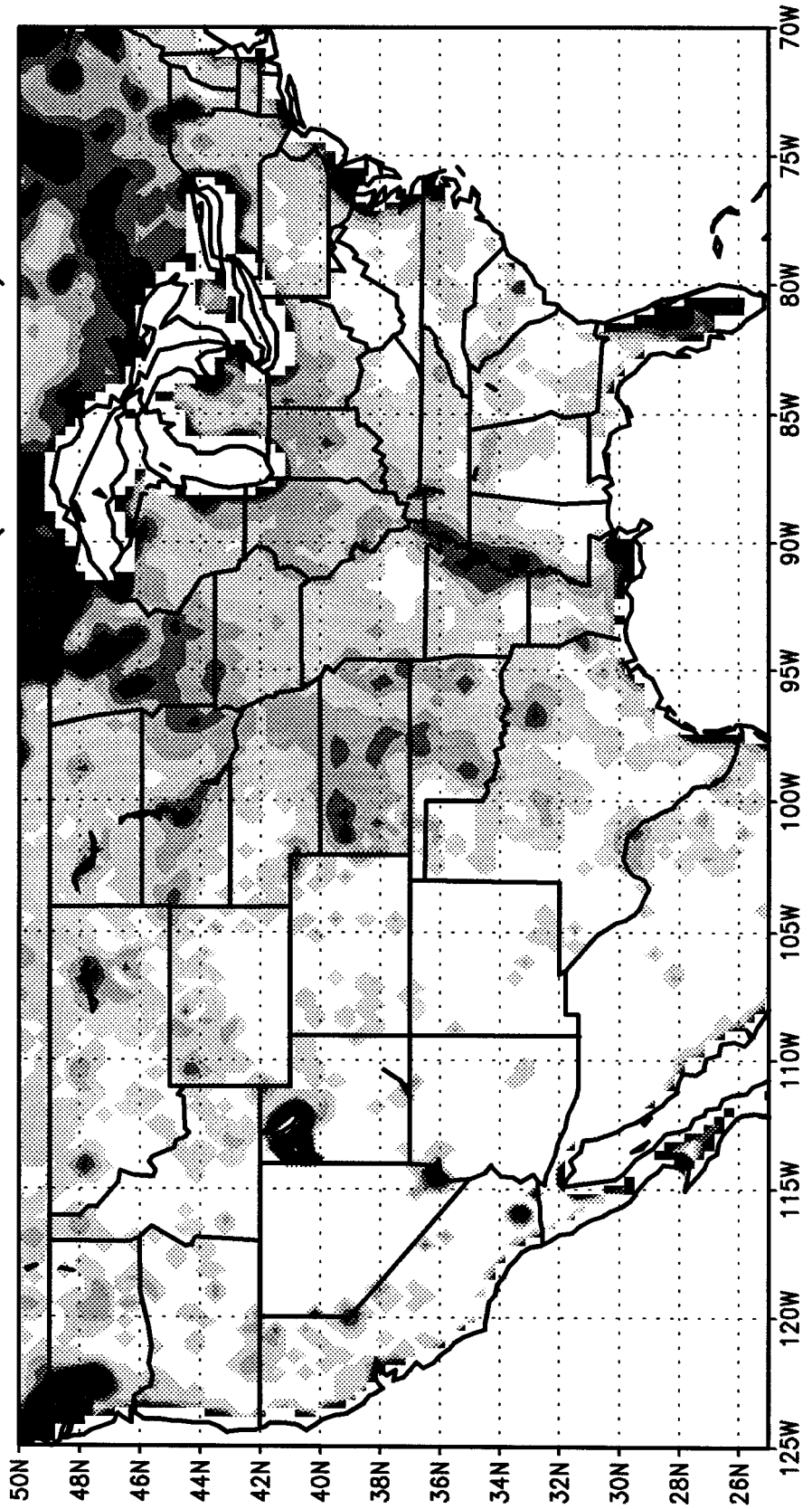

FIG. 9. The Basist wetness index (BWI) over the United States is added directly to the temperature in order to compensate for the lower emissivity at 19 GHz where the surface is wet. Note that the difference field between the temperature products is nearly orthogonal to the BWI.

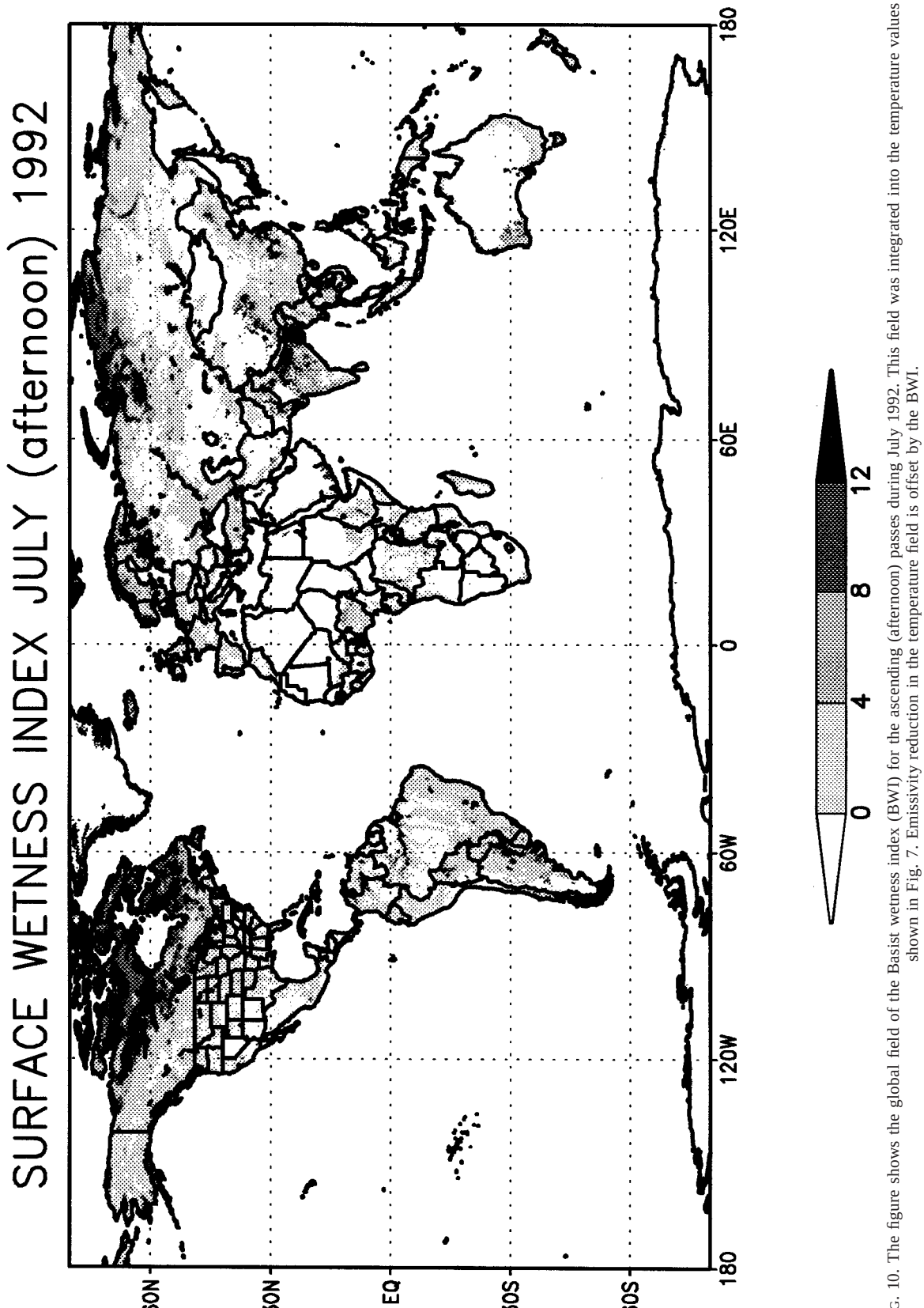

FIG. 10. The figure shows the global field of the Basist wetness index (BWI) for the ascending (afternoon) passes during July 1992. This field was integrated into the temperature values shown in Fig. 7. Emissivity reduction in the temperature field is offset by the BWI.

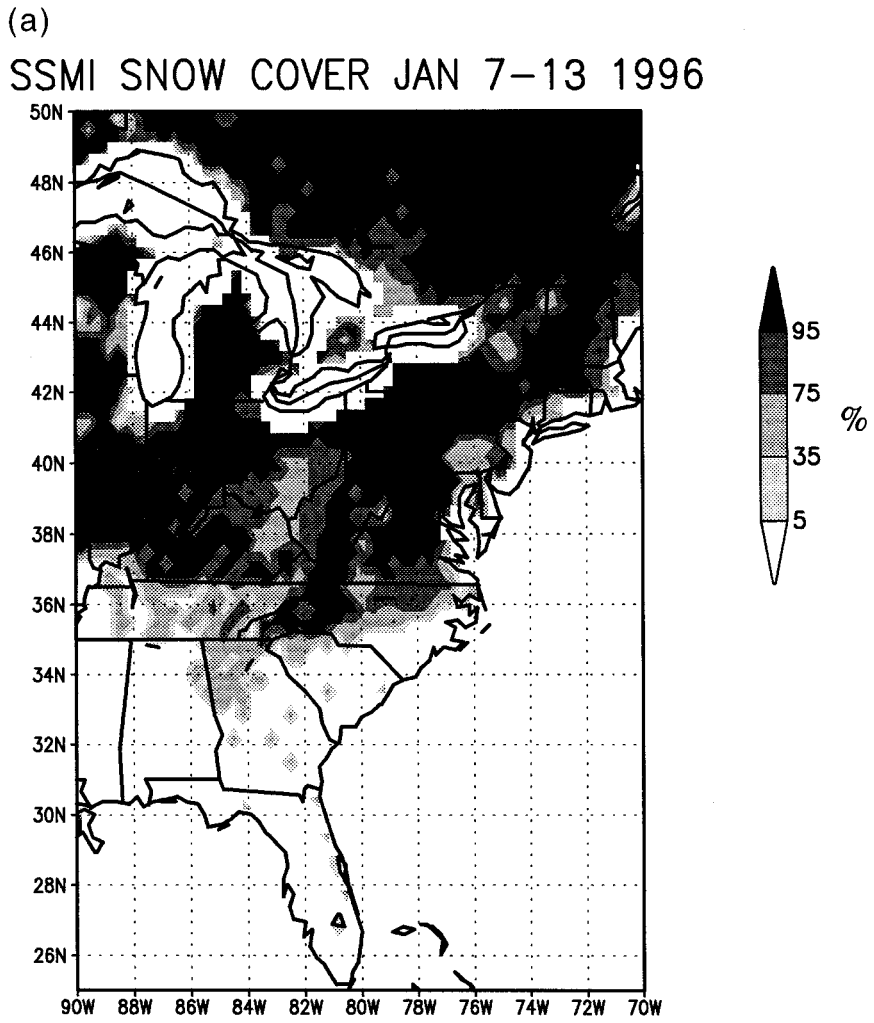

FIG. 11. (a) SSM/I-derived snow cover during the Blizzard of 1996, 7–13 January. (b) Snow cover during the week following the blizzard, 14–20 January, when unusually high temperatures and rain caused extensive floods. The values represent the percentage of the week when snow covered the ground. The product has low bias when the snowpack is melting.

vegetation, since the instrument cannot ''see'' through a dense canopy (a condition common along much of the eastern seaboard). Spatial patterns of the difference field and the BWI are largely orthogonal to the wetness field. In fact, the BWI gradient promotes smooth temperatures fields near the lower Mississippi and western Nebraska to the Texas panhandle (largely irrigated), as well as Minnesota. The difference between in situ and satellite temperatures over these areas are very small. The addition of the BWI significantly improves spatial correlations over wet surfaces. A land–sea tag is used to remove large water bodies from the index, since wetness index is intended to be a land surface product.

A map of the BWI values around the globe is presented in Fig. 10. The index identifies the location of the ITCZ over northern Africa and shows the monsoonal areas of Indian and southeastern Asia. The major river basins around the world (i.e., Amazon, Congo, Parana, and Mississippi) are also revealed. Note that the major tributaries of the Amazon are observed, but the dense surrounding forest does not appear wet, since the instrument cannot see through the canopy. Also the irrigated regions around numerous river valleys (i.e., Indus in Pakistan, Ganges in India, and Red River in China) are clearly detected. The global map has irregular patterns of large BWI values; however, when the BWI values are added to the temperature patterns, the resultant field is smooth. Specifically, observe the irregular BWI values over the tundra, where snowmelt tends to pool on the relatively flat surface and cannot penetrate the permafrost below. These values exceed 25 at some locations, yet the satellite-derived temperatures are quite smooth and realistic throughout the area.

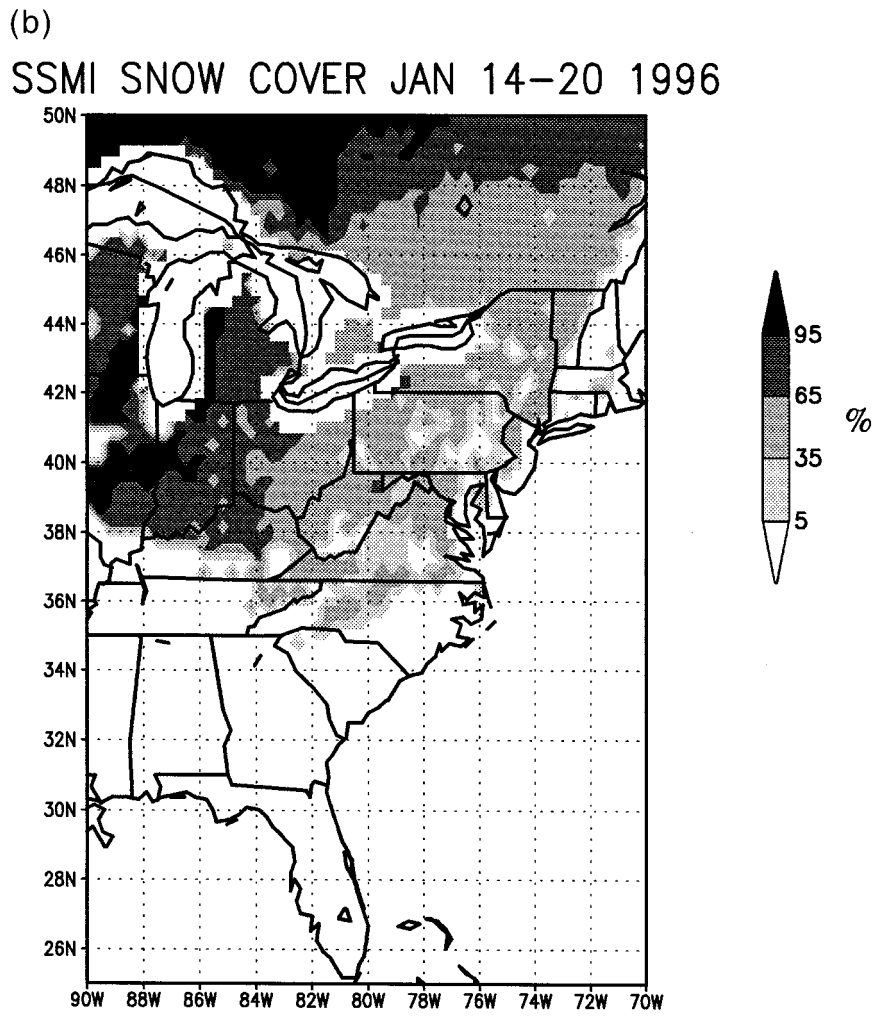

FIG. 11. (*Continued*)

b. Blizzard of 1996

During the week 7–13 January 1996 the eastern seaboard of the United States experienced one of its snowiest periods of the decade. The rain–snow line basically resided in the Carolinas, where numerous precipitation types (rain, freezing rain, sleet, and snow) were common. From Virginia northward most of the precipitation fell as snow and remained on the ground throughout the week. The heaviest snowfall occurred on Sunday, 7 January 1996 (when 50 cm was widespread), followed by lighter amounts during the next four days. Snowfall ended on Friday, 12 January 1996, and by this time an additional 25 cm was common. By the end of the week many locations from Virginia northward had snow depths in excess of 75 cm (U.S. Department of Commerce and U.S. Department of Agriculture 1996). Farther south in the Carolinas, a couple of freezing rain events followed by cold air advection kept the surface covered with an inch of ice. Deeper in the south, heavy rain corresponded with the snowfall farther north.

The following week brought record high temperatures along the eastern seaboard into southern Canada. This was further exacerbated by a major cold front on 19 January 1996 that produced severe thunderstorms and heavy rainfall up and down the eastern seaboard. Consequently the mass of snowcover underwent rapid melt, and many locations experienced severe flooding. By 20 January most of the snow over the mid-Atlantic states had melted away and a mass of cold Canadian air reestablished itself over the area (U.S. Department of Commerce and U.S. Department of Agriculture 1996).

Meteorological conditions during these two weeks brought persistent clouds, rain, freezing rain, fresh snow, metamorphosed snow, wet land, and flooded surfaces. We chose this case to test the strengths and limitations of our SSM/I-based algorithms to derive a wetness index, mean temperature, and snow cover under extreme conditions. This case study is further complicated by the implementation of a new instrument on the *F-13* satellite, whereas the algorithm and calibration

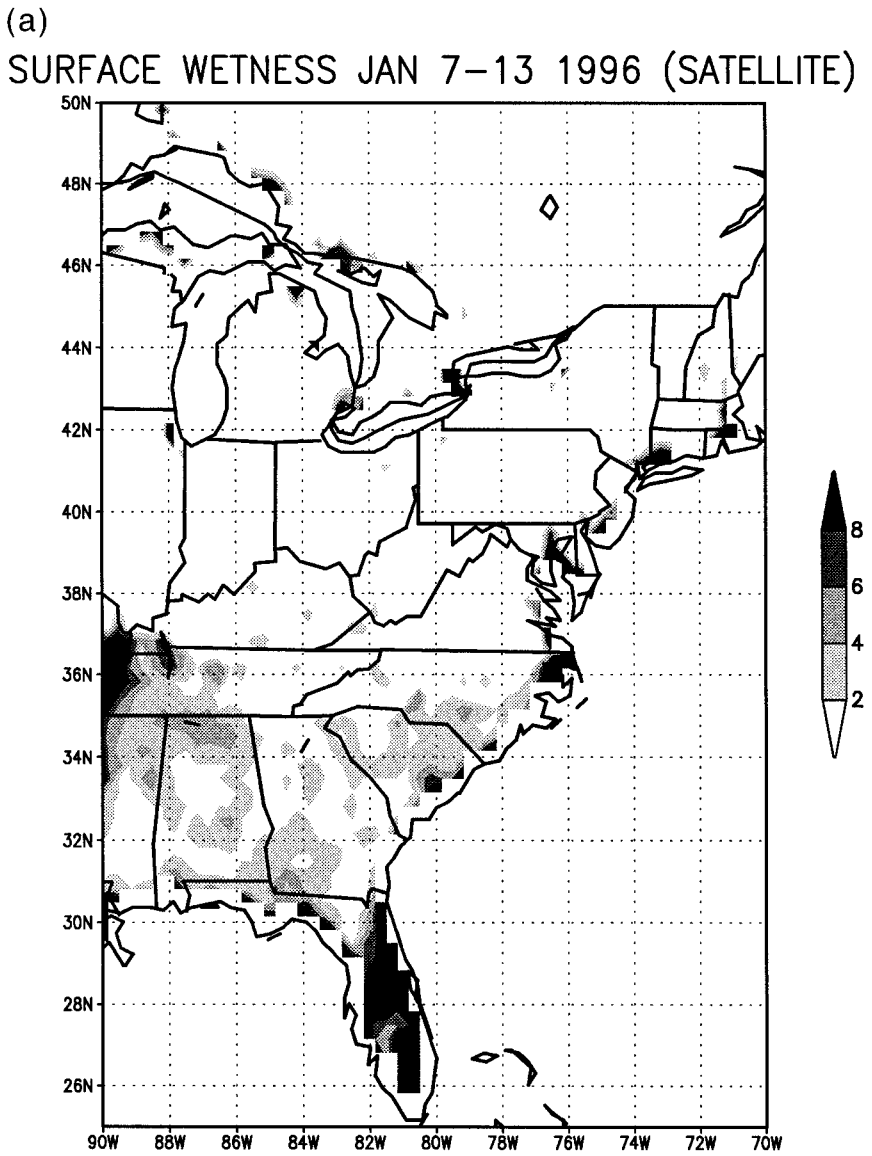

FIG. 12. The figure shows the BWI during (a) the Blizzard of 1996, and (b) the following week. Note the rain–snow line during the first week, as well as errors near the coastal margins. During the second week melting extended up to southern Canada, and there were floods in the mid-Atlantic states. The spatial patterns correspond to the surface type (e.g., the satellite cannot see wetness below a dry canopy).

were developed for the SSM/I instrument flown on the *F-11*. No intersatellite adjustment was implemented, since we concluded that it would be a way to test the algorithm's robustness to derive these parameters on different satellite platforms.

At the time of this analysis, only 800 real-time reporting stations were available for validation. The highest concentration of these observations (approximately 300) were in the eastern third of the country, where the Blizzard of 1996 occurred. Therefore, we restricted the study to this region. A map of snow cover for week one (Fig. 11a) indicates the persistent snow cover from the western Carolinas northward. Throughout this same area there are no wetness values (omitting contamination along a few coastal areas), since temperatures remained below freezing during the period. South of the snowpack the wetness value exceeds 6°C in some locations (Fig. 12a). The following week (14–20 January) brought above freezing temperatures up to southern Canada. The SSM/I snow cover product detects this January thaw (Fig. 11b), but it has a low bias, since it cannot detect snow cover when the pack is saturated with liquid water (Basist et al. 1996). (Realizing this weakness, only morning passes are used to monitor snow cover; yet, if

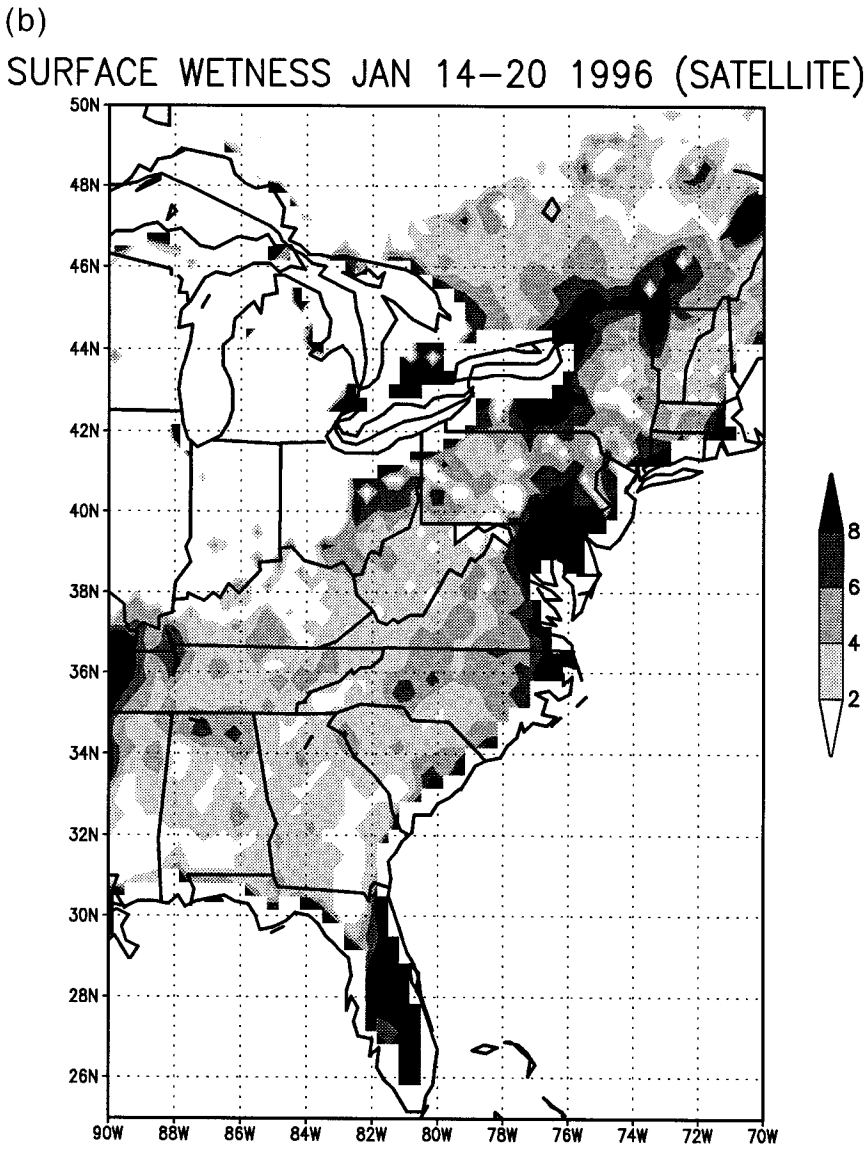

FIG. 12. (*Continued*)

temperatures do not drop below freezing by morning the low bias will persist.) The BWI detects the surface wetness (including melting snow) all the way up to southern Canada (Fig. 12b). Values exceeding 10 cover a portion of the mid-Atlantic region, the same area that experienced severe floods. The irregular characteristic of the index values correspond with locations of coniferous forests, where the wetness is obscured by the canopy. These BWI values were added to the T_b as indicated by (7) in order to derive the surface temperature over wet surfaces.

To test the accuracy of the satellite-derived temperatures during this period, both in situ and satellite temperatures are independently averaged into a 2-week composite, and compared. Even under these adverse conditions, temperature patterns generally correspond quite well (Figs. 13a,b). The unrealistically smooth pattern of the in situ data results from limited point values smoothed over the spatial domain. A difference map between these two fields shows both positive and negative patterns (Fig. 14). In situ observations over North Carolina indicate that the satellite product has a low bias during this event. As mentioned in section 3a, scattering resulting from freezing rain on the surfaces lowers the emissivity at all SSM/I frequencies, which is the origin of the cold bias over the region. Fortunately, when freezing rain covers the surface, the 85-GHz channel has a slightly higher T_b than the other frequencies. This knowledge gave us the ability to design an algorithm that identifies freezing rain and filters it out of future analyses. The high bias northward of North Carolina–Virginia border corresponds with light,

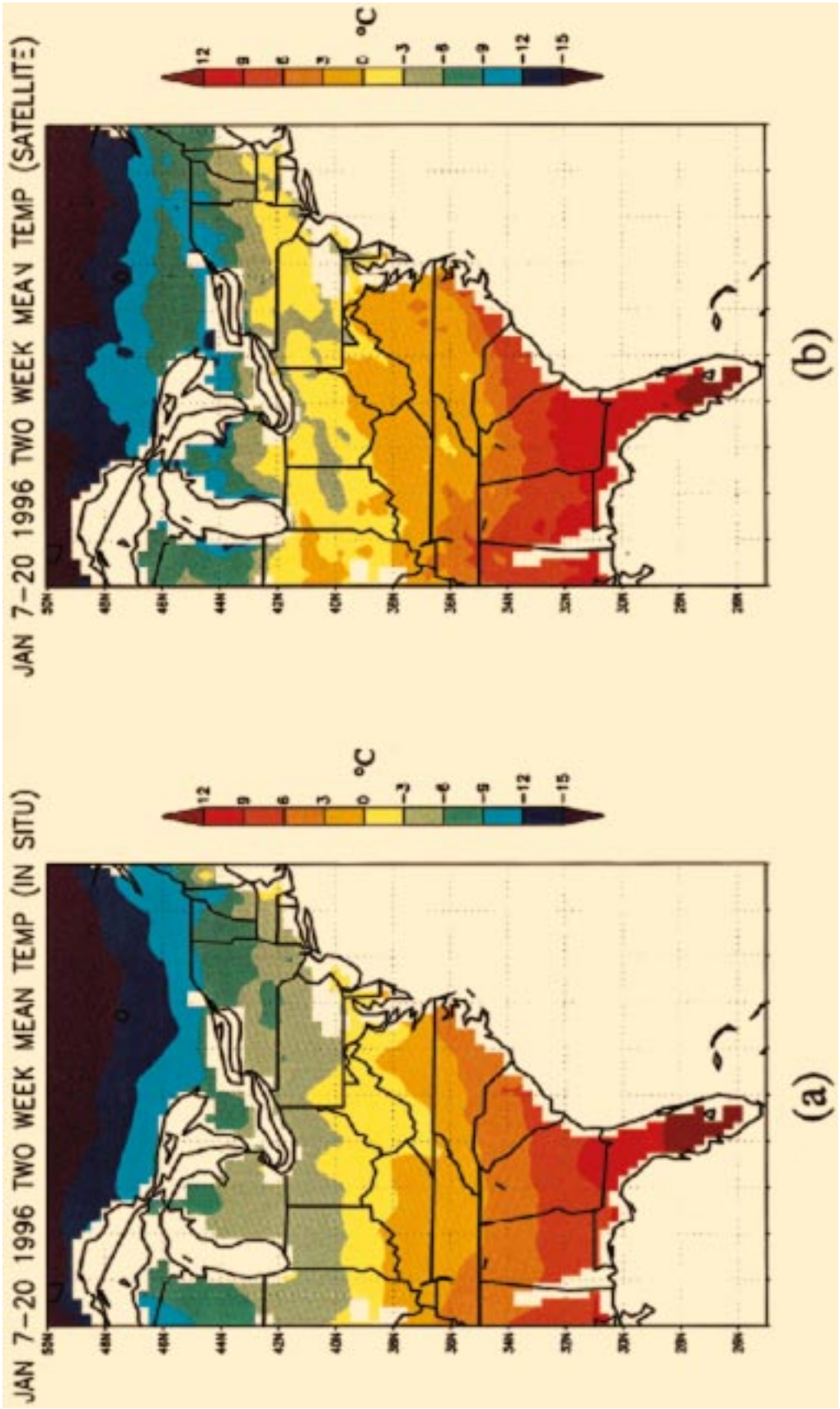

FIG. 13. (a) In situ shelter height, mean temperatures from the United States first-order stations gridded at 1° resolution over the period 7–20 January. (b) Satellite mean temperatures derived from the SSM/I channel values over the same period.

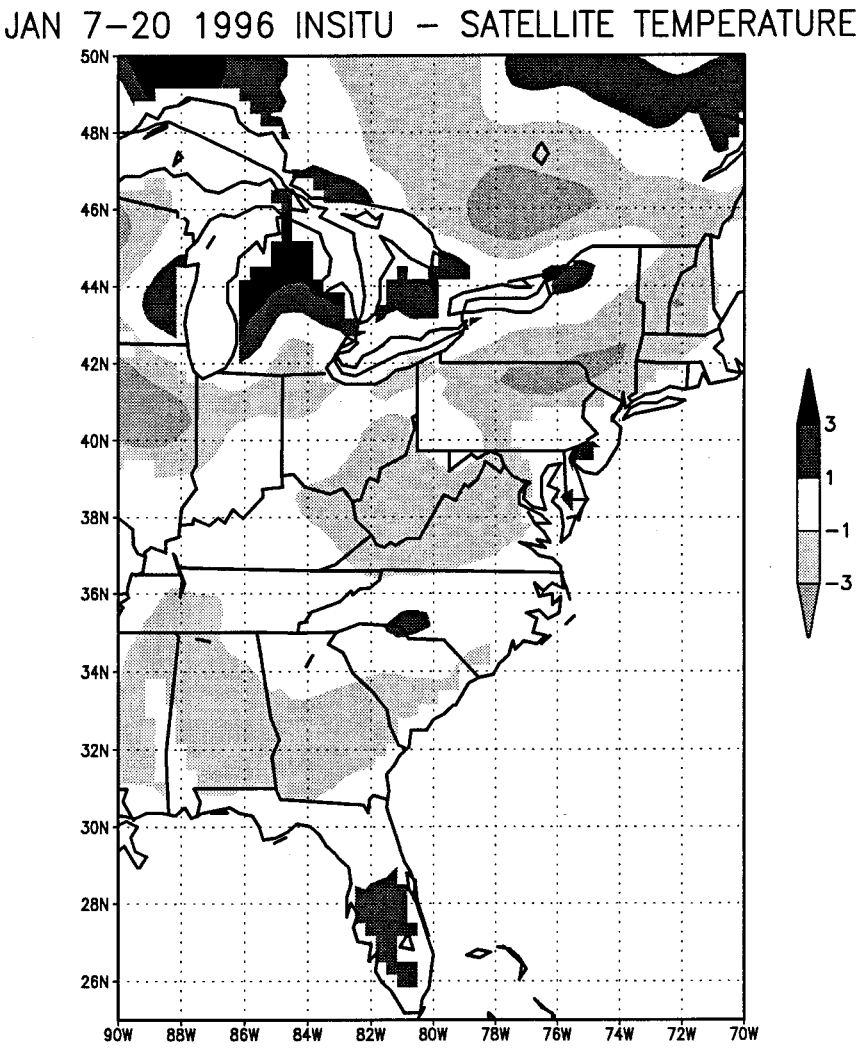

FIG. 14. The satellite–in situ difference field for the 2-week period 7–20 January. The cold satellite bias over the southeast corresponds to freezing rain. The high satellite bias comes from unknown origin. The greatest differences are present around the Great Lakes, where the snow was highly metamorphorized from coastal contamination. Generally, differences are less than 2°C, and in many areas they are less than 1°C.

low density snow. Under these conditions radiation received by the satellite instrument originates near the ground, which is insulated from the temperature on top of the snowpack. During much of this event, the temperature at the top of the snowpack was significantly below freezing, whereas the insulated ground stayed closer to the freezing point, producing the high bias. When the snow grains are small and of low density (relatively fresh snow) the 37-GHz channel exhibits very little scattering, whereas the 85-GHz channel displays a stronger scattering signature. When these conditions were present, the satellite-derived temperature will be filtered out of future analyses. The cold bias around the Great Lakes corresponds to metamorphosed snow cover, which scatters all the SSM/I frequencies. Since the 19-GHz channel also experiences scattering, the satellite temperatures appear colder than in situ. Metamorphosed snow scatters considerably more at 37 GHz than 85 GHz, which allows us to remove this snow type from future analyses. Before these three types of errors are filtered out of this analysis, there is a standard difference between the two datasets of 2.5°C. Even though there are considerable differences, both products place similar patterns of warm and cold temperatures, allowing the correlation between their spatial temperature fields to exceed 0.95.

When the three snow cover types (described in the paragraph above) are objectively removed from the analysis, temperatures throughout the snow-covered areas are filtered from the satellite product. Figure 15 shows the product for monthly mean minimum temperature for January 1996. Temperatures are calculated

over an area if more than 50% of the satellite data for the month passes through all the filters, including orbital gaps and/or data dropouts. The map correctly detects the temperature gradient up the eastern seaboard, while filtering out most of Canada and the high terrain of the Rocky Mountains. Note the smooth field over much of the western Amazon basin and the cold temperatures over the Andes highlands.

5. Blended satellite–in situ temperatures

The satellite and in situ values are blended to determine whether or not the resultant product would be superior to a stand-alone dataset. Anomaly interpolation from the surrounding grid points is a reliable way of filling in data-sparse regions (Willmott and Robson 1995). Therefore, we used monthly anomalies from the July 1992–95 base period, which spans two satellite instruments (*F-11* and *F-13*). The U.S. Cooperative Network of mean temperature data provided the in situ data. In this preliminary test there was ''no intercalibration'' between satellite platforms. (If results are encouraging with this crude test, they can only get better with a more refined approach.) To make sure we had adequate station data to produce robust grid-box anomaly values, we chose a $2^\circ \times 2^\circ$ grid and limited it from 33°–47°N, 114°–82°W. The interpolation was performed in both east–west and north–south directions.

In situ–derived anomalies were removed over certain regions, which allowed them to serve as independent ''ground truth'' in this analysis. Three different substitutions into these missing areas were performed: 1) straight in situ interpolation, 2) straight satellite-derived data, and 3) in situ interpolated values averaged with satellite-derived data. To provide a quick ''proof of concept'' on the advantage of blending the two fields, the blended product presented herein is based on a very simple approach. Figure 16 shows that the pure satellite-derived temperatures had the greater errors (an average rms error of 0.9°C) and in situ interpolation was next. Despite these satellite-derived errors, blending provided better results than in situ interpolation when distances exceeded 5° in the east–west coordinates, and more importantly, blending was better in the north–south coordinates at the 2° resolution.

6. Summary and conclusions

This article demonstrates the capability of the SSM/I instrument to observe land surface temperature throughout the United States and the globe. We developed a set of procedures that identify surface type and dynamically adjust the temperature for variations in surface emissivity. We also presented the inherent strengths and weaknesses in using passive microwave emission for observing surface temperature under a wide range of conditions. We compared the satellite temperature with high density in situ observations throughout the contiguous United States during July 1992. Generally the standard differences are around 2.0°C, and this value could drop considerably once the in situ values are adiabatically adjusted to mean SSM/I FOV elevation. Both the satellite and in situ fields had similar spatial patterns, although the satellite detected temperature gradient over data-sparse regions (deserts and mountains) that were absent in the in situ observations.

The Basist wetness index (BWI) accounts for the emissivity reduction associated with liquid water in the radiating surface. The index is used to identify surface wetness and to increase the 19-GHz brightness temperature to an emissivity of 0.945 (the nominal emissivity under dry conditions). The index identifies the major rivers, irrigated areas, and melting snow. During the Blizzard of 1996 the BWI identified the regions experiencing rainfall. It also identified the excessive melting and flooding during the week following the blizzard, when above normal temperatures and heavy rain dominated the eastern seaboard of North America.

When the temperature algorithm was tested on the *F-13* satellite platform during the Blizzard of 1996, it performed well, even though the algorithm was developed on the *F-11* satellite platform. Three land surface products (snow cover, surface wetness, and surface temperature) were monitored during this 2-week period. They all detected strong signals, which were also observed by independent in situ observations. However, the satellite-derived temperature did have considerable errors when snow cover exists, which we attribute to low frequency scattering due to freezing rain on surfaces and metamorphosed snow crystals. Subsequently these surface types have been identified and removed from the analysis.

We demonstrated that a blended satellite–in situ product could provide a better analysis than simple interpolation from in situ data alone (Xie and Arkin 1996). In the future we plan to blend satellite-derived surface temperature with the global network of in situ measurement available in near-real time on the Global Telecommunication System (Huffman et al. 1995). The spatial coherence pattern derived from the satellite-derived temperatures will be used to identify the gradient throughout areas of limited or absent in situ observations. The in situ values will serve as anchors for the satellite temperatures. The final product would be mean

→

FIG. 15. The figure shows the satellite-derived temperatures at 1° resolution for January 1996. Snow-covered surfaces are set to missing when pixels have unusual microwave signatures throughout the majority of the month. Otherwise, realistic temperature gradients across the region suggest that microwave frequencies can be used to identify temperature patterns over most surface and atmospheric conditions.

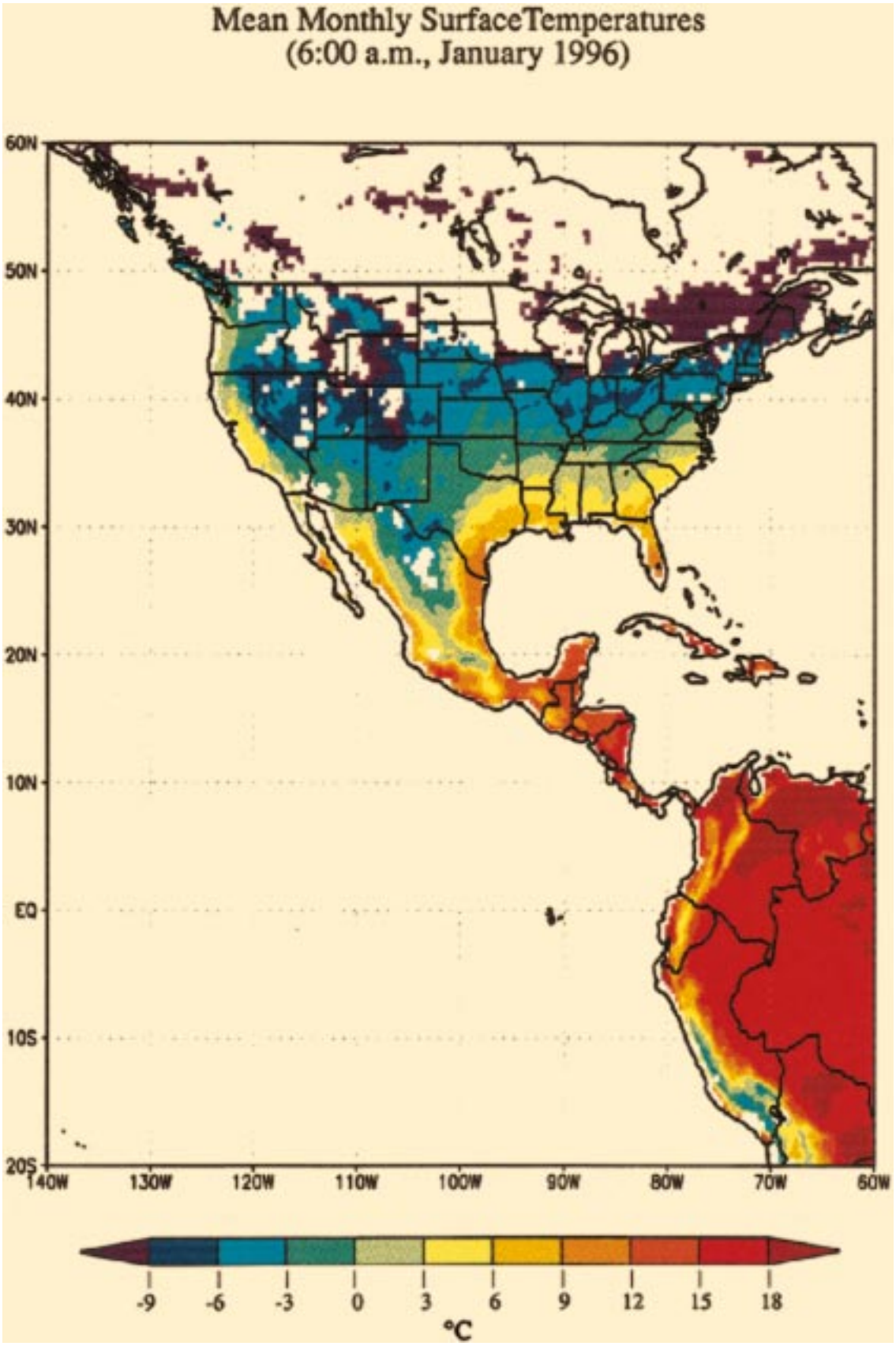
Mean Monthly SurfaceTemperatures
(6:00 a.m., January 1996)
60N
50N
40N
30N
20N
10N
EQ
10S
20S
140W
130W
120W
110W
100W
90W
80W
70W
60W
-9
-6
-3
0
3
6
9
12
15
18
°C

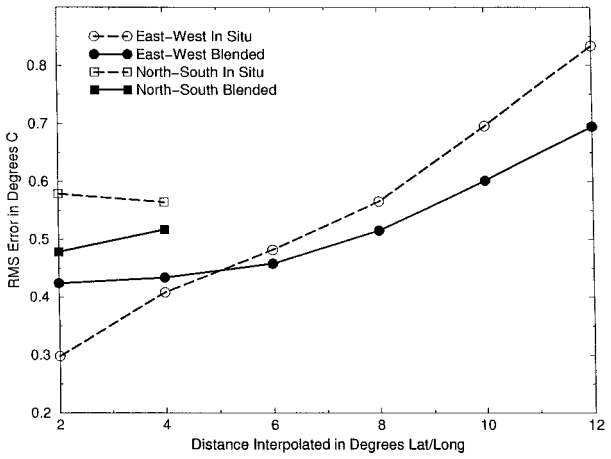

FIG. 16. Proof of concept that a blended in situ–satellite-derived temperature field is superior to in situ–only interpolation of temperature in data-sparse regions. The blended temperature has a lower root-mean-square error if the distance needed to be interpolated is greater than 5° in the east–west direction and 2° in the north–south direction. The data used are from the United States for July 1992–95 and gridded to 2° × 2° grid boxes.

monthly maximum, minimum, and mean temperatures, gridded to 1° resolution globally.

Our future work includes efforts to improve the current algorithm to observe land surface temperatures with the SSM/I instruments, use infrared values throughout snow-covered surfaces, utilize the International Satellite Cloud Climatology Project (ISSCP) gridded temperatures (Rossow and Zhang 1995) to determine the difference between the 1800 satellite overpass and maximum temperature, and investigate various techniques to blend satellite and in situ values into a superior product. We will work with Ignatov and Gutman (1998, manuscript submitted to *J. Climate*), who recently developed a technique to identify the diurnal temperature cycle from the ISCCP dataset.

Acknowledgments. Ralph Ferraro, who works in ORA/NESDIS, provided assistance in several aspects of this study. He supplied the SSM/I channel values that we used in the analysis. He helped develop the filters for convective rain. Futhermore, he provided guidance in the development of the algorithms for deriving surface temperaures from the suite of SSM/I frequencies. Support for this work has been provided by the NOAA Climate and Global Change Data and Detection program.

REFERENCES

Allison, L., 1977: Geological applications of nimbus radiation data in the Middle East. NASA Tech. Note TN D-8469, 79 pp. [Available from National Technical Information Service, Technology Administration, U.S. Department of Commerce, Springfield, VA 22161.]

Basist, A., and N. C. Grody, 1997: Surface wetness and snow cover. Preprints, *13th Conf. on Hydrology,* Long Beach, CA, Amer. Meteor. Soc., 190–193.

——, D. Garrett, N. C. Grody, R. R. Ferraro, and K. Mitchell, 1996: A comparison between snow cover products derived from visible and microwave satellite observations. *J. Appl. Meteor.*, **35,** 163–177.

Cambell, M., and J. Ulrichs, 1969: Electrical properties of rocks and their significance for lunar radar observations. *J. Geophys. Res.*, **74,** 5867–5881.

Cornett, W. M., and J. G. Shank, 1993: Impact of cirrus clouds on remote sensing of surface temperatures. *Proc. of SPIE,* Orlando, FL, SPIE, 252–263.

Davis, P. A., and J. D. Tarpley, 1983: Estimation of shelter temperatures from operational satellite sounder data. *J. Climate Appl. Meteor.*, **22,** 369–376.

Entekhabi, D., H. Nakamura, and E. G. Njoku, 1995: Solving the inverse problem for soil moisture and temperature profiles by sequential assimilation of multifrequency remotely sensed observations. *IEEE Trans. Geosci. Remote Sens.*, **32,** 438–448.

Ferraro, R., and G. F. Marks, 1994: Effects of surface conditions on rain identification using the SSM/I. *Remote Sens. Rev.*, **11,** 195–209.

——, and Coauthors, 1994: Microwave measurements produce global climatic, hydrologic data. *Eos, Trans. Amer. Geophys. Union,* **75** (30), 337–338, 343.

——, F. Weng, N. C. Grody, and A. Basist, 1996: An eight-year (1987–1994) time series of rainfall, clouds, water vapor, snow cover, and sea ice derived from SSM/I measurements. *Bull. Amer. Meteor. Soc.*, **77,** 891–905.

Grody, N. C., and A. Basist, 1996: Global identification of snow cover using SSM/I measurements. *IEEE Trans. Geosci. Remote Sens.*, **34,** 237–249.

——, and ——, 1997: Interpretation of SSM/I measurements over Greenland. *IEEE Trans. Geosci. Remote Sens.*, **35,** 360–366.

Groisman, P. Y., and F. L. Genikhovich, 1997: Assessing surface–atmosphere interactions using former Soviet Union standard meteorological network data. Part I: Method. *J. Climate,* **10,** 2154–2183.

Hall, F. G., K. F. Huemrich, S. J. Goetz, P. J. Sellers, and J. F. Nickeson, 1992: Satellite remote sensing of surface energy balance: Successes, failures, and unresolved issues in FIFE. *J. Geophys. Res.*, **97,** 19 061–19 089.

Halpert, M., Ed., 1994: Fifth annual climate assessment. National Centers of Environmental Prediction, 111 pp. [Available from Climate Prediction Center, 5200 Auth Rd., Camp Springs, MD 20746.]

Hollinger, J. R., B. Lo, G. Poe, R. Savage, and J. Pierce, 1987: Special Sensor Microwave user's guide. Naval Research Lab Tech. Rep., Washington, DC, 119 pp.

Huffman, G. J., R. F. Adler, B. Rudolf, U. Schneider, and P. R. Keehn, 1995: Global precipitation estimates based on a technique for combining satellite-based estimates, rain gauge analysis, and NWP model precipitation information. *J. Climate,* **8,** 1284–1295.

Jones, A. S., and T. H. Vonder Haar, 1997: Retrieval of microwave surface emittance over land using coincident microwave and infrared satellite measurements. *J. Geophys. Res.*, **102,** 13 609–13 626.

Karl, T. R., R. W. Knight, and J. R. Christy, 1994: Global and hemispheric temperature trends: Uncertainties related to inadequate spatial sampling. *J. Climate,* **7,** 1144–1163.

Lettenmaier, D. P., 1994: Hydro-climatological trends in the continental United States, 1948–88. *J. Climate,* **7,** 586–607.

Matzler, C., 1994: Passive microwave signatures of landscapes in winter. *Meteor. Atmos. Phys.*, **54,** 241–260.

McFarland, J. M., R. L. Miller, and C. M. U. Neale, 1990: Land surface temperature derived from the SSM/I passive microwave brightness temperatures. *IEEE Trans. Geosci. Remote Sens.*, **28,** 839–845.

Myneni, R. B., and B. J. Choudhury, 1993: Synergistic use of optical

and microwave data in agrimeteorological applications. *Adv. Space Res.,* **13,** 239–248.

Neale, C. M. U., M. J. McFarland, and K. Chang, 1990: Land-surface-type classification using microwave brightness temperatures from the Special Sensor Microwave/Imager. *IEEE Trans. Geosci. Remote Sens.,* **28,** 829–238.

Njoku, E. G., 1994: Surface temperature estimation over land using satellite microwave radiometry. *Remote Sensing of Land–Atmosphere Interactions,* P. Pampolini, Ed., VSP, 509–530.

Reynolds, R. W., and T. M. Smith, 1994: Improved sea surface temperatures using optimal interpolation. *J. Climate,* **7,** 929–948.

Rizzi, R., 1994: Cloud clearing of infrared sounder radiance. *J. Appl. Meteor.,* **33,** 179–194.

Rossow, W. B., and L. C. Garder, 1993: Validation of ISCCP cloud detections. *J. Climate,* **6,** 2370–2393.

——, and Y. C. Zhang, 1995: Calculation of surface and top of atmosphere radiative fluxes from physical quantities based on ISCCP data sets. 2: Validation and first results. *J. Geophys. Res.,* **100,** 1167–1197.

Trenberth, K. E., J. R. Christy, and J. W. Hurrell, 1992: Monitoring global monthly mean surface temperatures. *J. Climate,* **5,** 1405–1423.

Tsang, W. L., J. R. Wang., and P. C. Doraiswamy, 1993: Relationship between satellite microwave radiometric data, antecedent precipitation index, and regional soil moisture. *Int. J. Remote Sens.,* **14,** 2483–2500.

U.S. Department of Commerce and U.S. Department of Agriculture, 1996: *Weekly Wea. Crop Bull.,* **83** (2), 32 pp.

Vidal, A., 1991: Atmospheric and emissivity correction of land surface temperature measured from satellite using ground measurements of satellite data. *Int. J. Remote Sens.,* **12,** 2449–2460.

Wang, R., and T. J. Schmugge, 1980: An empirical model for the complex dielectric permittivity of soil as a function of water content. *IEEE Trans. Geosci. Remote Sens.,* **18,** 288–295.

Willmott, C. J., and S. M. Robson, 1995: Climatologically aided interpolation (CAI) of terrestrial air temperature. *Int. J. Climatol.,* **15,** 221–229.

Xie, P., and P. Arkin, 1996: Analyses of global monthly precipitation using gauge observations, satellite estimates, and numerical model predictions. *J. Climate,* **9,** 840–858.